The LISA DFACS: A nonlinear model for the spacecraft dynamics

The LISA DFACS: a Nonlinear Model for the Spacecraft Dynamics[⋆,⋆⋆]

Simone Vidano[a,*], Carlo Novara[a], Luigi Colangelo[a], Jonathan Grzymisch[b]

[a] *Department of Electronics and Telecommunications, Politecnico di Torino, Corso Duca degli Abruzzi 24, Turin 10129, Italy*
[b] *Guidance, Navigation and Control Section (TEC-SAG), ESTEC, European Space Agency, Keplerlaan 1, Noordwijk 2201 AZ, The Netherlands*

Abstract

In the last few years, the observation of gravitational waves by means of LIGO and Virgo interferometers and the success of LISA Pathfinder, gave a significant boost to the development of space-based gravitational wave observatories. The European Space Agency confirmed LISA as the third large class mission of the Cosmic Vision program. The present work is part of the Drag Free and Attitude Control System (DFACS) preliminary prototyping study, which aims at the development of mathematical models and advanced controllers for the science phases of the LISA mission. Nonlinear modelling is a fundamental step for the derivation of linearized and decoupled models as well as for the development of suitable linear and nonlinear controllers. In this paper, an analytical nonlinear model is derived, which describes all the relevant dynamics of a LISA spacecraft, representing an effective compromise between accuracy and complexity. The model is extensively validated through linearization analysis and Monte Carlo simulations.

Keywords: LISA, drag-free, spacecraft, multibody, dynamics, modelling

Nomenclature

Acronyms

AME	Arithmetic Mean Error
CRF	Constellation Reference Frame
DFACS	Drag Free Attitude Control System
DWS	Differential Wavefront Sensing
DoF	Degree of Freedom
ESA	European Space Agency
ES	Electrostatic Suspension
FEEP	Field Emission Electric Propulsion

⋆This work is part of the LISA DFACS preliminary prototyping study under the European Space Agency Technology Development Element program.

⋆⋆Partial contents of this paper were presented in the 69th International Astronautical Congress, as paper IAC-18,C1,6,4,x47173, held in Oct. 2018, Bremen, Germany. This is an improved and extended version.

*Corresponding author

Email addresses: simone.vidano@polito.it (Simone Vidano), carlo.novara@polito.it (Carlo Novara), luigi.colangelo@polito.it (Luigi Colangelo), jonathan.grzymisch@esa.int (Jonathan Grzymisch)

GRS Gravitational Reference Sensor

IF Interferometer

IRF Inertial Reference Frame

LISA Laser Interferometer Space Antenna

MIMO Multi Input Multi Output

MRF Mass Reference Frame

MPS Micro Propulsion System

RMSE Root Mean Square Error

OA Optical Assembly

ORF Optical Reference Frame

SC Spacecraft

SRF Spacecraft Reference Frame

STR Star Tracker

TM Test Mass

Variables

$\mathbf{r}_I \in \mathbb{R}^3$: S/C CoM position wrt the IRF origin - components in IRF

$\mathbf{r}_M \in \mathbb{R}^3$: TM CoM position wrt the cage center - components in ORF

$\mathbf{r}_M^I \in \mathbb{R}^3$: TM CoM position wrt the cage center - components in IRF

$\mathbf{r}_{MI} \in \mathbb{R}^3$: TM CoM position wrt the IRF origin - components in IRF

$\mathfrak{q}_S \in \mathbb{R}^4$: quaternion of the rotation CRF –> SRF

$\mathfrak{q}_{SI} \in \mathbb{R}^4$: quaternion of the rotation IRF –> SRF

$\mathfrak{q}_\zeta \in \mathbb{R}^4$: quaternion of the rotation SRF –> ORF

$\mathfrak{q}_M \in \mathbb{R}^4$: quaternion of the rotation ORF –> MRF

$\boldsymbol{\theta}_S \in \mathbb{R}^3$: Euler angle vector of the rotation CRF –> SRF

$\boldsymbol{\theta}_M \in \mathbb{R}^3$: Euler angle vector of the rotation ORF –> MRF

$\boldsymbol{\omega}_S \in \mathbb{R}^3$: S/C angular velocity wrt CRF - components in SRF

$\boldsymbol{\omega}_{SI} \in \mathbb{R}^3$: S/C angular velocity wrt IRF - components in SRF

$\boldsymbol{\omega}_O \in \mathbb{R}^3$: OA angular velocity wrt IRF - components in ORF

$\boldsymbol{\omega}_M \in \mathbb{R}^3$: TM angular velocity w.r.t. ORF - components in MRF

$\boldsymbol{\omega}_{MI} \in \mathbb{R}^3$: TM angular velocity w.r.t. IRF - components in MRF

$\boldsymbol{\omega}_C \in \mathbb{R}^3$: CRF origin angular velocity wrt IRF - components in CRF

$\gamma \in \mathbb{R}^1$: angle between the ORF x-axis and the SRF x-axis

$\zeta \in \mathbb{R}^1$: angle between the ORF x-axis and its direction at rest

$\boldsymbol{\omega}_\zeta \doteq (0, 0, \dot{\zeta}),\ \boldsymbol{\omega}_\gamma \doteq (0, 0, \dot{\gamma})$

$\boldsymbol{\alpha}_\zeta \doteq (0, 0, \ddot{\zeta}),\ \boldsymbol{\alpha}_\gamma \doteq (0, 0, \ddot{\gamma})$

$\boldsymbol{L}_2$,$\boldsymbol{L}_3$: direction vectors of the laser rays coming from SC2 and SC3 on SC1.

Command inputs

$\mathbf{F}_T \in \mathbb{R}^3$: MPS command force - components in SRF

$\mathbf{F}_E \in \mathbb{R}^3$: ES force - components in ORF

$\mathbf{M}_T \in \mathbb{R}^3$: MPS torque - components in SRF

$\mathbf{M}_E \in \mathbb{R}^3$: ES torque - components in ORF

$\mathrm{M}_{OA} \in \mathbb{R}$: OA command torque

Disturbances

$\mathbf{d}_S \in \mathbb{R}^3$: disturbance force acting on a S/C - components in SRF

$\mathbf{d}_M \in \mathbb{R}^3$: disturbance force acting on a TM - components in ORF

$\mathbf{D}_S \in \mathbb{R}^3$: disturbance torque acting on a S/C - components in SRF

$\mathbf{D}_M \in \mathbb{R}^3$: disturbance torque acting on a TM - components in ORF

$\mathrm{D}_\zeta \in \mathbb{R}$: disturbance torque acting on an OA

$\mathbf{F}_{St} \in \mathbb{R}^3$: stiffness force acting on a TM - components in ORF

$\mathbf{M}_{St} \in \mathbb{R}^3$: stiffness torque acting on a TM - components in ORF

Parameters

$m_S \in \mathbb{R}^1$: S/C mass (including the two OAs)

$m_M \in \mathbb{R}^1$: TM mass

$J_S \in \mathbb{R}^{3\times3}$: S/C inertia matrix w.r.t its CoM (including the two OAs)

$\mathbf{b}_S \in \mathbb{R}^3$: vector from the S/C CoM to the OA pivot - components in SRF

$\mathbf{b}_M \in \mathbb{R}^3$: vector from the OA pivot to the cage center - components in ORF

$\mathbf{b} \equiv \mathbf{b}_S + T_O^S \mathbf{b}_M \in \mathbb{R}^3$: vector from the S/C CoM to the cage center - components in SRF

$K_t, c_t, I_{zz} \in \mathbb{R}^1$: OA stiffness, damping, inertia

Mathematical Notations

- Scalars: $a, b \in \mathbb{R}$.
- Column vectors:
$$\mathbf{r} = (r_1, \ldots, r_n) = [r_1 \ \ldots \ r_n]^T = \begin{bmatrix} r_1 \\ \vdots \\ r_n \end{bmatrix} \in \mathbb{R}^{n\times1}.$$
- Row vectors: $\mathbf{r}^T = [r_1 \ \ldots \ r_n] \in \mathbb{R}^{1\times n}$.
- Matrices: $M \in \mathbb{R}^{n\times m}$.
- Cross products:
$$\mathbf{r} \times \mathbf{p} = \begin{bmatrix} 0 & -r_3 & r_2 \\ r_3 & 0 & -r_1 \\ -r_2 & r_1 & 0 \end{bmatrix} \begin{bmatrix} p_1 \\ p_2 \\ p_3 \end{bmatrix} = \begin{bmatrix} r_2p_3 - r_3p_2 \\ r_3p_1 - r_1p_3 \\ r_1p_2 - r_2p_1 \end{bmatrix}$$
$$\mathbf{r}^\times \doteq \begin{bmatrix} 0 & -r_3 & r_2 \\ r_3 & 0 & -r_1 \\ -r_2 & r_1 & 0 \end{bmatrix}.$$
- Vector ℓ_2 (Euclidean) norm:
$$|\mathbf{r}| = \|\mathbf{r}\| = \|\mathbf{r}\|_2 = \sqrt{\mathbf{r}\cdot\mathbf{r}} = \sqrt{\mathbf{r}^T\mathbf{r}} = \sqrt{\textstyle\sum_{i=1}^n r_i^2} = r.$$
- $\Lambda(\boldsymbol{\omega}) \equiv \Lambda(J, \boldsymbol{\omega}) \doteq -J^{-1}\boldsymbol{\omega} \times J\boldsymbol{\omega}$.
- $\boldsymbol{\Omega} \equiv \boldsymbol{\Omega}(\boldsymbol{\omega}) \doteq \boldsymbol{\omega}^\times\boldsymbol{\omega}^\times + \dot{\boldsymbol{\omega}}^\times$.
- $Z(\gamma)$ elementary rotation around z-axis by an angle γ.

- T_a^b: rotation matrix RFb –> RFa (coordinate transformation RFa –> RFb). A rotation matrix can be expressed in function of the corresponding quaternion as

$$T \equiv T(\mathfrak{q}) = \begin{bmatrix} q_0^2+q_1^2-q_2^2-q_3^2 & 2(q_1q_2-q_0q_3) & 2(q_1q_3+q_0q_2) \\ 2(q_1q_2+q_0q_3) & q_0^2-q_1^2+q_2^2-q_3^2 & 2(q_2q_3-q_0q_1) \\ 2(q_1q_3-q_0q_2) & 2(q_2q_3+q_0q_1) & q_0^2-q_1^2-q_2^2+q_3^2 \end{bmatrix}.$$

- Rotation matrix time derivative (Poisson relation):

$$\begin{aligned} \dot{T}_a^b &= T_a^b \boldsymbol{\omega}_a \times \\ \dot{T}_b^a &= -\boldsymbol{\omega}_a \times T_b^a \end{aligned} \tag{1}$$

where $\boldsymbol{\omega}$ is the angular velocity vector of RFa wrt RFb with components expressed in RFa.

- Quaternions: $\mathfrak{q} = (q_0, \mathbf{q}) = \begin{bmatrix} q_0 \\ \mathbf{q} \end{bmatrix}$, $q_0 \in \mathbb{R}$, $\mathbf{q} \in \mathbb{R}^{3\times 1}$.
- Quaternion product: $\mathfrak{q} \otimes \mathfrak{p} = (q_0p_0 - \mathbf{q}\cdot\mathbf{p}) + (q_0\mathbf{p} + p_0\mathbf{q} + \mathbf{q}\times\mathbf{p})$
- Quaternion kinematics matrix:

$$Q(\mathfrak{q}) \doteq \begin{bmatrix} -q_1 & -q_2 & -q_3 \\ q_0 & -q_3 & q_2 \\ q_3 & q_0 & -q_1 \\ -q_2 & q_1 & q_0 \end{bmatrix}$$

- Quaternion to Euler 123 conversion:

$$\begin{aligned} \varphi &= \operatorname{atan2}\left(-\frac{2\left(q_3q_4 - q_0q_1\right)}{q_0^2 - q_1^2 - q_2^2 + q_4^2}\right) \\ \vartheta &= \operatorname{asin}\left(q_1q_3 + q_0q_2\right) \\ \psi &= \operatorname{atan2}\left(-\frac{2\left(q_1q_2 - q_0q_3\right)}{q_0^2 + q_1^2 - q_2^2 - q_4^2}\right) \end{aligned} \tag{2}$$

1. Introduction

Gravitational waves are an important aspect of General Relativity Theory that still needs to be fully investigated. For this reason, LIGO and Virgo ground-based interferometers were set up in the mid-1990s and were improved in the following decades [1], achieving the first observation of a gravitational wave in 2015 [2]. The Earth's seismic activity affects their measurement spectrum below 10 Hz [1] and consequently, the gravitational waves emitted by some astrophysical objects cannot be observed [3]. The first concept of a space-based interferometer, with a measurement bandwidth from 0.02 mHz up to 1 Hz, was proposed in the mid-1990s [4], but due to the overall complexity and the uncertainties regarding the current state of the art of technology, a precursor mission of LISA was developed in the mid-2000s [5, 6, 7]. LISA Pathfinder was launched in 2015 and performed in-orbit tests until 2017, demonstrating key technologies required to satisfy LISA performance requirements [8].

These outcomes, together with the first observations of gravitational waves by means of ground-based interferometers, resulted in the selection of LISA as the third large class mission in the next ESA Cosmic Vision program. Hence, as part of the mission preparation, ESA started several development studies such as the system Phase-A and the LISA DFACS (Drag Free and Attitude Control System). In the meanwhile, academic research mainly focused on spacecraft rendezvous [9, 10], formation control [11, 12] and flexible spacecrafts [13, 14] rather than drag-free controls. The latter are necessary in all the applications that require a fine compensation of the disturbances affecting science and for this reason they were used in the past for gravimetry missions such as GOCE [15] and GRACE [16]. However, drag-free control is of primary importance also for the obsevation of gravitational waves, which are detected by measuring accurately the relative distance between two bodies placed in geodesic trajectories. This condition can only be obtained by compensating for all the disturbances acting on the reference bodies down to the nanoscopic scale by means of a high performance drag-free controller.

The present work is part of the LISA DFACS preliminary prototyping study, which aims at the mathematical modelling of the spacecraft dynamics and at the design of controllers for the science phases of the LISA mission. Despite some papers on control systems for past LISA concepts are present in the literature [17, 18], very limited information is available on the mathematical models. For instance, [17] provides some guidelines for a possible drag free control system, but no information regarding mathematical modelling is shown. [18] provides a linear state space model used for the control design, but neither its derivation nor the terms that compose the model are reported. The same holds for the modelling and control design papers about LISA Pathfinder [19, 20, 21]. Another difference with respect to the previous works about LISA is that they consider an old spacecraft concept that dates back to the mid-2000s. For example, [18] assumes different spacecraft mass and inertia properties, different actuators (FEEP instead of cold gas thrusters) and different noises.

In the present work, the latest spacecraft concept is reviewed, then reference systems are defined and an algorithm to obtain the so called Constellation Reference Frame is provided. A nonlinear model for the multi-body dynamics is derived and validated in simulation. To the best of the Authors' knowledge, it is the first complete nonlinear dynamic model available in the literature for a LISA spacecraft. It describes all the relevant nonlinearities, representing an effective compromise between accuracy and complexity. It is not computationally demanding allowing quite fast simulation and it is suitable for linearization, decoupling and control design. A preliminary version of the model was presented by the Authors in [22]. With respect to [22], the present paper provides an improved version of the model, its derivation, the validation process and the analysis of the results. Moreover, an algorithm for the computation of the constellation frame is proposed.

2. Methodology

The LISA spacecraft is a quite complex multi-body system and consequently cannot be modelled and controlled as a simple rigid body. The spacecraft concept was reviewed in order to identify the bodies involved, the degrees of freedom and the kinematic chains. Then, suitable reference systems were assigned to the plant and a nonlinear model was obtained by means of a Newton-Euler approach. In order to validate the model,

the frequency and the time responses were evaluated in Matlab-Simulink and compared with a SimScape multi-body benchmark model. SimScape is a CAD-like software based on Matlab-Simulink that allows to build models of complex physical systems using a set of elementary blocks, avoiding the use of mathematical equations. Although the SimScape model is accurate in simulating the spacecraft dynamics, it does not provide a mathematical description of the system that is being modelled.

3. Nonlinear modelling

3.1. Plant Description

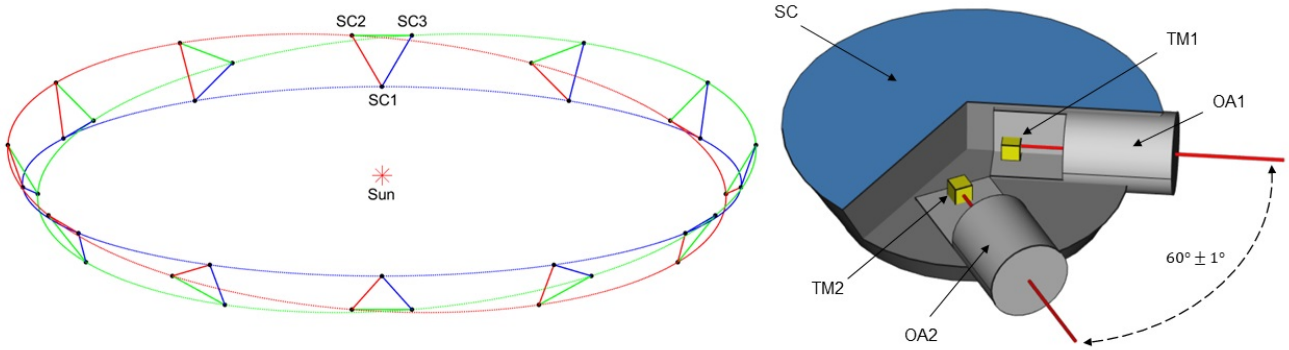

Figure 1: LISA orbits (left), LISA spacecraft (right)

The LISA observatory consists in a constellation of three spacecraft travelling on different inclined heliocentric orbits, resulting in a Sun-facing spinning triangle with a nominal side length of $2.5 \cdot 10^6$ km (Fig. 1). Due to the orbital dynamics, the inner angles change periodically between 59° and 61° and the constellation center follows the Earth at an average distance of $60 \cdot 10^6$ km.

The current spacecraft concept consists of a science module that carries two moving Optical Assemblies (OA) whose nominal inter-angle is 60° (Fig. 1). In turn, each OA is composed by: i) a telescope; ii) an optical bench for laser interferometry; iii) an electrostatic suspension system (also known as Gravitational Reference Sensor), which houses a suspended cubic test mass (TM) as shown in Fig. 2. The GRS was tested in-orbit by LISA Pathfinder [23], [24] and will be inherited by LISA.

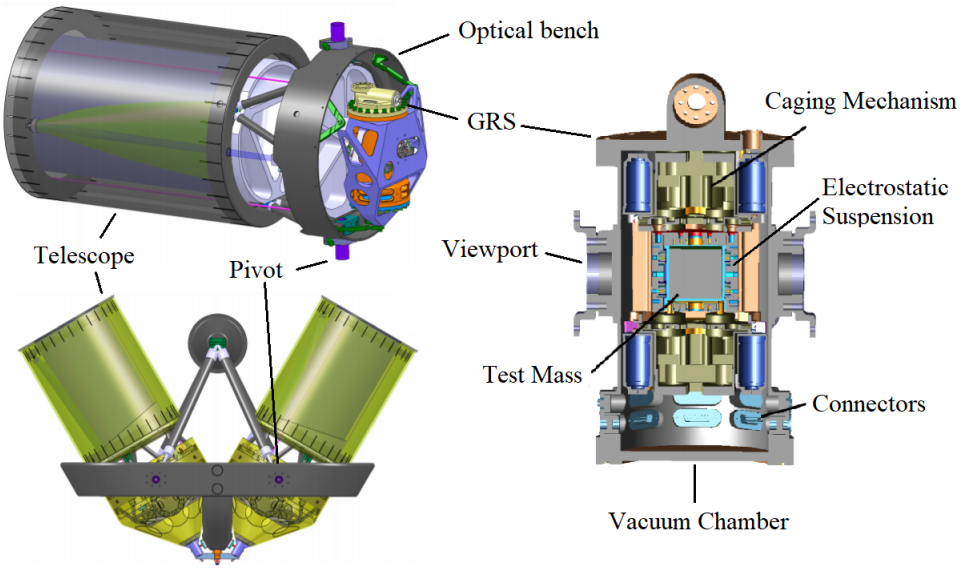

Figure 2: Optical Assembly (left), Gravitational Reference Sensor (right) [25]

The spacecraft is also a well-balanced system, given its geometrical symmetry and mass distribution, such that the overall center of mass is close to the barycentre.

Since the LISA control problem is based on nanoscopic scale quantities, some low-scale couplings that affect the system dynamics are not negligible. For instance, even if the test masses are apparently unconnected and suspended inside the spacecraft, the local electromagnetic and gravitational fields determine low-scale interactions between spacecraft and test mass that act as virtual springs. This problem has been addressed also in LISA Pathfinder [26] and in some other preliminary studies about LISA [27].

Hence, eacmass is stiffly connected to the optical assembly with a system of virtual springs, while each OA is linked to the main body thanks to a mechanical hinge that allows only yaw movements. To conclude, a single LISA spacecraft is a multi-body system characterized by 20 degrees of freedom: (i) 6 DoFs for the external body; (ii) 1 DoF for each optical assembly; (iii) 6 DoFs for each test mass.

Depending on the mission phase, several configurations of actuators and sensors will be available. For what concerns the actuators, cold gas thrusters are mounted on the external surface and apply forces/torques directly on the main body. The inter-telescope angle is commanded by means of a dedicated internal actuator that applies torques around the mechanical hinges of the telescopes. All the TM DoFs can be controlled and sensed thanks to the electrostatic suspension. The longitudinal translation, the pitch and yaw angles of the two test masses can be also measured through laser interferometry techniques. The spacecraft inertial attitude is measured only out of science mode, since the available star trackers are expected to be too noisy and inaccurate for science purposes. Conversely, during science mode and when the constellation laser links have been acquired, the spacecraft attitude relative to the incoming laser wavefronts is measured by means of the Differential Wavefront Sensing (DWS) interferometry techniques.

For what concerns the environmental disturbances, the solar pressure acts on the external SC body, while test masses are affected by the SC gravitational field and by other low-scale disturbances [28].

To sum up, LISA is a 20x17 MIMO system, whose command inputs and measured outputs are summarized

in Table 1 and Table 2.

Name	Variable	Dim.	Notes
MPS force	$\mathbf{F}_T$	3	The spacecraft body is controlled by means of the MPS, a set of 9 cold gas thrusters arranged in three different pods around the spacecraft lateral surface. The MPS can provide thrust and torque in order to control every DoF of the spacecraft body.
MPS torque	$\mathbf{M}_T$	3	
OA1 torque	M_{OA1}	1	Each optical assembly can be rotated around its pivot by a dedicated motor. This command torque allows to control the opening angle between the two optical assemblies in order to keep the laser links of the constellation. Since the OA are fixed to the spacecraft body, the reaction torque of the optical assemblies will be applied on the spacecraft body.
OA2 torque	M_{OA2}	1	
TM1 force	$\mathbf{F}_{E1}$	3	Each test mass is controlled by the GRS, which contains an electrostatic suspension able to control all the 6 DoF. Since the GRS is mounted on the OA, the reaction forces and torques of the electrostatic suspension will be applied to the OA and the spacecraft.
TM1 torque	$\mathbf{M}_{E1}$	3	
TM2 force	$\mathbf{F}_{E2}$	3	
TM2 torque	$\mathbf{M}_{E2}$	3	

Table 1: LISA command inputs

Name	Variable	Dim.	Notes
SC inertial attitude	$\boldsymbol{\theta}_{SI}$	3	The inertial attitude is measured only out of science mode by means of a system of star trackers.
SC attitude	$\boldsymbol{\theta}_S$	3	During the drag free mode, the DWS provides the azimuth and elevation angles of the incoming laser beams. These measurements can be used to reconstruct the constellation frame and the SC attitude relative to this frame.
TM1 position	$\mathbf{r}_{M1}$	3	The first electrostatic suspension (ES1) measures the TM1 position relative to the cage center. During drag free mode, the local interferometer is used to measure the longitudinal displacement (x-coordinate) of the test mass.
TM1 attitude	$\boldsymbol{\theta}_{M1}$	3	ES1 measures TM1 attitude with respect to the cage frame. DWS interferometry techniques provide finer measurements of the test mass pitch and yaw.
TM2 position	$\mathbf{r}_{M2}$	3	Same as TM1 position
TM2 attitude	$\boldsymbol{\theta}_{M2}$	3	Same as TM1 attitude
OA1 angle	ζ_1	1	OA1 opening angle with respect to the rest position.
OA2 angle	ζ_2	1	OA2 opening angle with respect to the rest position.

Table 2: LISA measured outputs

3.2. Reference Systems

3.2.1. Definition

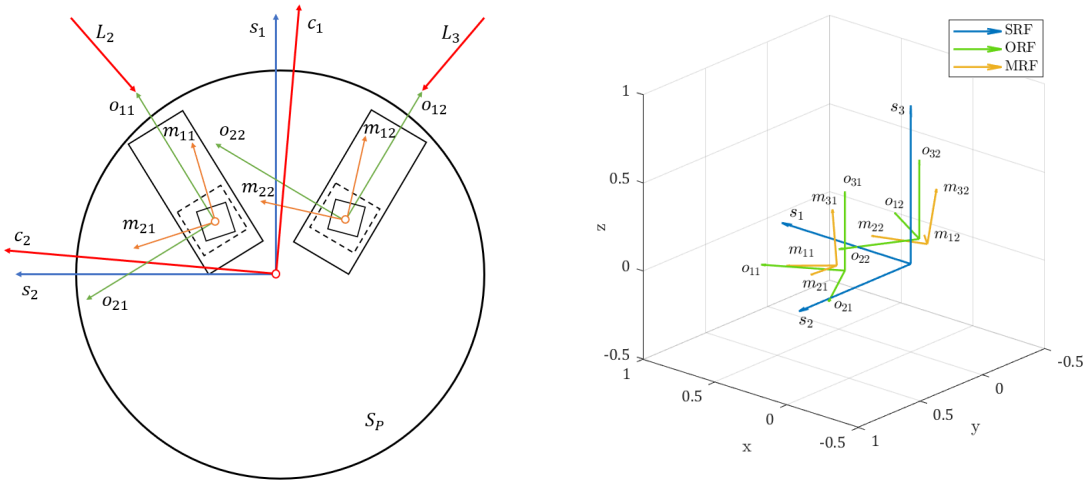

Figure 3: Spacecraft frame:$\{\boldsymbol{s}_1, \boldsymbol{s}_2, \boldsymbol{s}_3\}$, Optical Assembly frame: $\{\boldsymbol{o}_{1i}, \boldsymbol{o}_{2i}, \boldsymbol{o}_{3i}\}$, Test Mass frame: $\{\boldsymbol{m}_{1i}, \boldsymbol{m}_{2i}, \boldsymbol{m}_{3i}\}$, Constellation frame:$\{\boldsymbol{c}_1, \boldsymbol{c}_2, \boldsymbol{c}_3\}$, S_P: solar panel plane, $\boldsymbol{L}_2\boldsymbol{L}_3$: incoming laser rays

The LISA spacecraft is composed by 5 main bodies and consequently at least 7 reference frames have to be defined. The main reference frames (i.e. for SC1) are:

- The Sun-centered Inertial Reference Frame: $IRF = \{O_I, \boldsymbol{I}_1, \boldsymbol{I}_2, \boldsymbol{I}_3\}$
- The Constellation Reference Frame: $CRF = \{O_C, \boldsymbol{c}_1, \boldsymbol{c}_2, \boldsymbol{c}_3\}$

  Reconstructed on-board starting from the incoming laser directions. It is centered on the spacecraft barycentre, $\boldsymbol{c}_3$ is perpendicular to the plane that contains the laser vectors $\boldsymbol{L}_2$ and $\boldsymbol{L}_3$, $\boldsymbol{c}_1$ is the bisector of the angle defined by the incoming laser directions.

- The Spacecraft Reference Frame: $SRF = \{O_S, \boldsymbol{s}_1, \boldsymbol{s}_2, \boldsymbol{s}_3\}$

  Centered on the spacecraft barycentre, $\boldsymbol{s}_1$ is the bisector of the nominal inter-telescope angle $\alpha = \pi/3$, $\boldsymbol{s}_3$ is perpendicular to the solar panel S_P.

- Two Optical Reference Frames: $ORFi = \{O_{Oi}, \boldsymbol{o}_{1i}, \boldsymbol{o}_{2i}, \boldsymbol{o}_{3i}\}$ where $i = 1$ for the left optical assembly and $i = 2$ for the right one.

  The origin of the i-th frame is located at the cage center of the corresponding electrostatic suspension. For what concerns the frame axes, the following condition holds: $\boldsymbol{o}_{31} \| \boldsymbol{o}_{32} \| \boldsymbol{s}_3$. Moreover, $\boldsymbol{o}_{1i}$ is parallel to the symmetry axis of the corresponding optical assembly.

- Two Test-Mass Reference Frames: $MRFi = \{O_{Mi}, \boldsymbol{m}_{1i}, \boldsymbol{m}_{2i}, \boldsymbol{m}_{3i}\}$ where $i = 1$ for the left test mass and $i = 2$ for the right one.

  Each frame is centered on the CoM of the corresponding test-mass, $\boldsymbol{m}_{1i}, \boldsymbol{m}_{2i}, \boldsymbol{m}_{3i}$ are orthogonal to the TM faces.

3.2.2. The Constellation Reference Frame

During science mode, the star tracker is not available and consequently the SC attitude with respect to the IRF cannot be measured. Hence, for SC attitude control purposes it is convenient to consider also the Constellation Reference Frame $CRF = \{O_C, \boldsymbol{c}_1, \boldsymbol{c}_2, \boldsymbol{c}_3\}$, whose $\boldsymbol{c}_1$ axis is the bisetrix of the angle defined by the incoming laser rays and $\boldsymbol{c}_3$ is perpendicular to the laser plane P, which is defined by the laser ray directions $\boldsymbol{L}_2$ and $\boldsymbol{L}_3$. The CRF can be reconstructed on-board thanks to the long arm DWS sensors, which provide the azimuth and elevation angles of the incoming laser rays with respect to the optical reference frames. A possible algorithm is reported hereafter.

The first step consists in computing the laser ray vectors by means of the well known formula of the spherical coordinate systems and then make a change of coordinates from the ORF to the SRF. Let be φ_k and ϑ_k the azimuth and elevation angles of the laser coming from the k-th SC to the i-th ORF:

$$\boldsymbol{L}_k = T_{Oi}^{S} \begin{bmatrix} \sin(\varphi_k)\cos(\vartheta_k) \\ \cos(\varphi_k)\cos(\vartheta_k) \\ \sin(\vartheta_k) \end{bmatrix}, \quad k = 2,3 \quad i = 1,2.$$

Then, the equation of the plane P that contains $\boldsymbol{L}_2$ and $\boldsymbol{L}_3$ is computed by means of a cross product. This provides not only the coefficients of the cartesian equation, but also the normal vector, which corresponds to the z-axis of the constellation frame:

$$\boldsymbol{L}_2 \times \boldsymbol{L}_3 = \begin{bmatrix} a & b & c \end{bmatrix}^T$$

$$P : ax + by + cz = 0$$

$$\boldsymbol{c}_3 = \frac{\boldsymbol{L}_2 \times \boldsymbol{L}_3}{\|\boldsymbol{L}_2 \times \boldsymbol{L}_3\|} = \frac{\begin{bmatrix} a & b & c \end{bmatrix}^T}{\sqrt{a^2+b^2+c^2}}.$$

However, there exists an infinite number of orthonormal bases whose x and y axes lie on the plane P. Hence, another constraint has to be set in order to obtain the constellation frame. The $\boldsymbol{c}_1$ axis has to be the bisector of the angle between $\boldsymbol{L}_2$ and $\boldsymbol{L}_3$ on the plane P:

$$\boldsymbol{L}_2 = \begin{bmatrix} x_2 & y_2 & z_2 \end{bmatrix}^T \quad \boldsymbol{L}_3 = \begin{bmatrix} x_3 & y_3 & z_3 \end{bmatrix}^T \quad A = \sum_{i=2}^{3} \frac{x_i}{\sqrt{x_i^2+y_i^2}} \quad B = \sum_{i=2}^{3} \frac{y_i}{\sqrt{x_i^2+y_i^2}} \quad C = \sum_{i=2}^{3} \frac{z_i}{\sqrt{x_i^2+y_i^2}}$$

$$\boldsymbol{c}_1 = \frac{\begin{bmatrix} A & B & C \end{bmatrix}^T}{\sqrt{A^2+B^2+C^2}}.$$

Finally, $\boldsymbol{c}_2$ can be computed as the cross product between $\boldsymbol{c}_3$ and $\boldsymbol{c}_1$.The final result is shown in Figure 4.

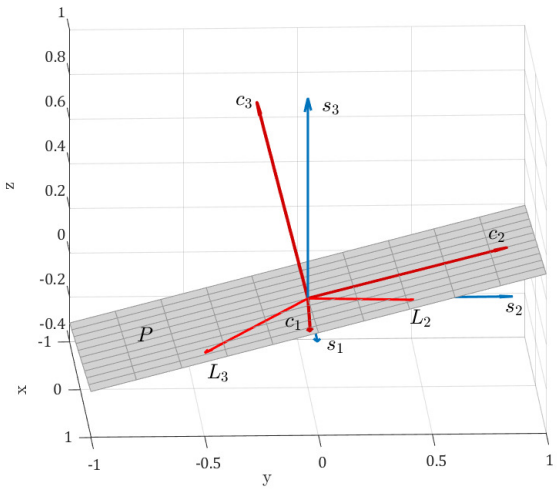

Figure 4: Constellation Reference Frame ($\{O_C, \boldsymbol{c}_1, \boldsymbol{c}_2, \boldsymbol{c}_3\}$) and Spacecraft Reference Frame ($\{O_S, \boldsymbol{s}_1, \boldsymbol{s}_2, \boldsymbol{s}_3\}$)

3.3. Nonlinear Model

From the control design point of view, it is important to have a simple, but representative dynamic model. As a matter of fact, the complexity increases the design effort, the possibility of implementation errors and it could be also a limiting factor for the applicability of certain control techniques. The nonlinear model presented in this study is based on some reasonable assumptions:

1. Given the symmetry and the balancing of the spacecraft concept, the CoM is assumed to lie on the SRF origin and this allows to simplify the equation of motion. The Newton-Euler equations with respect to a certain reference frame whose origin is not located on the center of mass are given by [29]:

$$\begin{bmatrix} \mathbf{F} \\ \mathbf{T} \end{bmatrix} = \begin{bmatrix} mI & -m\mathbf{r}_C^{\times} \\ m\mathbf{r}_C^{\times} & J - m\mathbf{r}_C^{\times}\mathbf{r}_C^{\times} \end{bmatrix} \begin{bmatrix} \ddot{\mathbf{r}}_o \\ \dot{\boldsymbol{\omega}}_o \end{bmatrix} + \begin{bmatrix} m\,\boldsymbol{\omega}^{\times}\boldsymbol{\omega}^{\times}\mathbf{r}_C \\ \boldsymbol{\omega}^{\times}\left(J - m\,\mathbf{r}_C^{\times}\mathbf{r}_C^{\times}\right)\boldsymbol{\omega} \end{bmatrix} \tag{3}$$

   where the left-hand side are the forces and the torques acting on the body, the right hand side collects all the inertial and fictitius force terms, $\ddot{\mathbf{r}}_o$ and $\dot{\boldsymbol{\omega}}_o$ are the frame translational and angular accelerations, $\mathbf{r}_C$ is the distance between the frame origin and the center of mass. When $\mathbf{r}_C = \mathbf{0}$ some terms of (3) become null.
2. Given the high manufacturing tollerances demonstrated by LISA Pathfinder, the test mass is assumed to be an ideal cube whose mass is homogeneously distributed. Therefore, the center of mass, the barycenter and the MRF origin are assumed to be coincident, providing further simplification of the equation of motion for the same reason of point 1.
3. The two optical assemblies are currently under system study, but in any case their connection with the spacecraft body shall be sufficiently rigid in order to avoid excessive oscillations that could affect science. A 1 DoF second order model made by a torsional mass spring damper system can be considered.
4. The OAs will be used to track the pulsation of the constellation angle, which is expected to be maximum 1° with a very slow rate of $1.15 \cdot 10^{-7}$ °/s. Hence, the effects of the OA dynamics on the spacecraft and

on the test mass should not be relevant. Moreover, eventual motion cross-couplings to other coordinates can be neglected.

In this section, the nonlinear model is presented through four main subsections: the spacecraft attitude dynamics, the OA model, the TM attitude dynamics and the relative translation dynamics between SC and TM. Figure 5 shows a vector scheme helpful to understand the nonlinear equations.

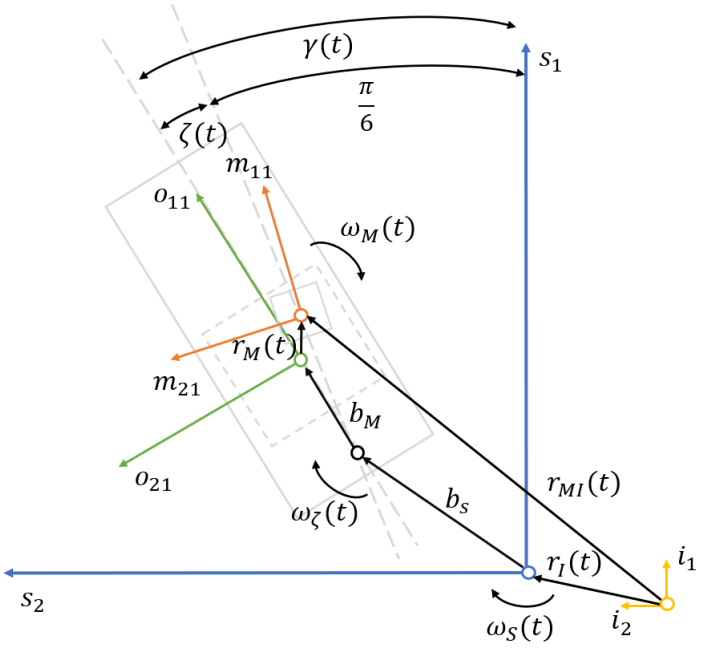

Figure 5: Vector scheme for TM1

3.3.1. SC Attitude Dynamics

The goal of the LISA attitude control during science, is to align the SRF with the CRF. Hence, a rotation dynamics model that describes the SC attitude relative to the CRF is needed. Let us consider the notations and definitions section at the beginning of the present paper. According to the addition rule of the angular velocities,

$$\boldsymbol{\omega}_S = \boldsymbol{\omega}_{SI} - T_C^S \boldsymbol{\omega}_C \tag{4}$$

where $\boldsymbol{\omega}_S$ is the SC angular velocity with respect to the constellation frame in SRF components, $\boldsymbol{\omega}_{SI}$ is the SC inertial angular velocity in SRF components and $\boldsymbol{\omega}_C$ is the angular velocity of the constellation frame in CRF components. The SC angular acceleration relative to the CRF can be obtained by means of the time derivative of (4) and by considering (1):

$$\begin{aligned} \dot{\boldsymbol{\omega}}_S &= \dot{\boldsymbol{\omega}}_{SI} - \dot{T}_C^S \boldsymbol{\omega}_C - T_C^S \dot{\boldsymbol{\omega}}_C \\ &= \dot{\boldsymbol{\omega}}_{SI} + \boldsymbol{\omega}_S \times T_C^S \boldsymbol{\omega}_C - T_C^S \dot{\boldsymbol{\omega}}_C, \end{aligned} \tag{5}$$

where the inertial angular acceleration $\dot{\boldsymbol{\omega}}_{SI}$ is given by the Euler equation

$$\dot{\boldsymbol{\omega}}_{SI} = -J_S^{-1}\boldsymbol{\omega}_{SI} \times J_S\boldsymbol{\omega}_{SI} + J_S^{-1}\left(\mathbf{M}_T + \mathbf{D}_S - \sum_{j=1,2}\left(T_{Oj}^S I_{zz}\ddot{\boldsymbol{\zeta}}_j + T_{Oj}^S\mathbf{M}_{Ej} + \mathbf{b}_j \times T_{Oj}^S\mathbf{F}_{Ej}\right)\right). \tag{6}$$

$\mathbf{M}_T$ is the total torque of the thrusters, $\mathbf{D}_S$ is the resultant torque of all the external disturbances acting on the SC body (i.e. the solar pressure), while the other terms are the reactions of the internal actuators (i.e. the optical assemblies and the electrostatic suspensions). In particular, $\mathbf{M}_{Ej}$ are the electrostatic torques used to control the attitude of the j-th TM and $\mathbf{F}_{Ej}$ are the electrostatic forces used to control the TM translation. Since each suspension cage is located at a distance $\mathbf{b}_j$ from the SRF origin, also $\mathbf{F}_{Ej}$ generate torques that affect the spacecraft attitude. The rotation matrix $T_C^S = T(\mathfrak{q}_S^*)$ is time-variant and depends on the spacecraft attitude quaternion, while the rotation matrices $T_{Oj}^S = Z(\gamma_j)$ are time-variant since they are function of the OA opening angles γ_j ($\zeta_j(t)$):

$$\gamma_j(t) = \begin{cases} \pi/6 + \zeta_j(t), & j = 1 \\ -\pi/6 + \zeta_j(t), & j = 2. \end{cases} \quad \forall\, t \geq t_0\ . \tag{7}$$

By replacing (6) into (5), it is possible to obtain the complete expression of the spacecraft angular acceleration relative to the constellation frame in SRF components. To conclude, the SC attitude dynamics model is:

$$\begin{aligned} \dot{\boldsymbol{\omega}}_S &= \dot{\boldsymbol{\omega}}_{SI} + \boldsymbol{\omega}_S \times T_C^S\boldsymbol{\omega}_C - T_C^S\dot{\boldsymbol{\omega}}_C \\ \dot{\boldsymbol{\omega}}_{SI} &= -J_S^{-1}\boldsymbol{\omega}_{SI} \times J_S\boldsymbol{\omega}_{SI} + J_S^{-1}\left(\mathbf{M}_T + \mathbf{D}_S - \sum_{i=1,2}\left(T_{Oj}^S I_{zz}\ddot{\boldsymbol{\zeta}}_j + T_{Oi}^S\mathbf{M}_{Ej} + \mathbf{b}_i \times T_{Oi}^S\mathbf{F}_{Ej}\right)\right) \\ \dot{\mathfrak{q}}_S &= \frac{1}{2}\mathfrak{q}_S \otimes \boldsymbol{\omega}_{S\mathfrak{q}} = \frac{1}{2}Q(\mathfrak{q}_S)\boldsymbol{\omega}_{S\mathfrak{q}}, \end{aligned} \tag{8}$$

where the attitude quaternion $\dot{\mathfrak{q}}_S$ is obtained from the angular velocity $\boldsymbol{\omega}_{S\mathfrak{q}} = (0, \boldsymbol{\omega}_S)$ by integrating the standard quaternion kinematics equation [30]. Since the thrusters provide a torque which is three/four orders of magnitude higher than the electrostatic suspension forces and torques, the reaction terms could be neglected for a even more simplified model.

When the star trackers are available outside the science mode, the inertial attitude quaternion $\mathfrak{q}_{SI}$ can be measured and an attitude dynamics model with respect to the IRF can be considered:

$$\dot{\mathfrak{q}}_{SI} = \frac{1}{2}\mathfrak{q}_{SI} \otimes \boldsymbol{\omega}_{SI\mathfrak{q}} = \frac{1}{2}Q(\mathfrak{q}_{SI})\boldsymbol{\omega}_{SI\mathfrak{q}}. \tag{9}$$

The attitude angles $\boldsymbol{\theta}_{SI}$ can be easily obtained from $\mathfrak{q}_{SI}$ thorugh (2).

3.3.2. OA model

The optical assemblies are currently under system study. Therefore, a preliminary second-order model can be considered to describe the yaw dynamics of the j-th OA:

$$\begin{aligned} \ddot{\boldsymbol{\zeta}}_j &= -2\omega_N \xi \dot{\boldsymbol{\zeta}}_j - \omega_N^2 \boldsymbol{\zeta}_j + \frac{M_{OAj}}{I_{zz}} - \frac{M_{Ej}}{I_{zz}} - T_S^{Oj}\dot{\boldsymbol{\omega}}_{SI} + \frac{\mathrm{D}_{\zeta j}}{I_{zz}} \\ \omega_N &= \sqrt{\frac{K_t}{I_{zz}}} \\ \xi &= \frac{c_t}{2\sqrt{K_t I_{zz}}}, \end{aligned} \tag{10}$$

where $\boldsymbol{\zeta}$ is the angle with respect to the direction at rest, K_t, c_t, I_{zz} are the stiffness, damping and inertia properties around the pivot axis. M_{OA} is the command torque provided by the OA motor, M_E is the reaction torque of the electrostatic suspension and $T_S^{Oj}\dot{\boldsymbol{\omega}}_{SI}$ are the effects of the spacecraft dynamics on the OA.

3.3.3. S/C-TM stiffness model

Before describing the TM rotation dynamics, it is important to provide a mathematical model for the low-scale couplings mentioned in Section 3.1 that are proportional to the test mass displacements $\mathbf{r}_M$ and $\boldsymbol{\vartheta}_M$. Therefore, they can be modelled as a system of virtual springs:

$$\begin{bmatrix} \mathbf{F}_{St} \\ \mathbf{M}_{St} \end{bmatrix} = \begin{bmatrix} S_{TT} & S_{RT} \\ S_{TR} & S_{RR} \end{bmatrix} \begin{bmatrix} \mathbf{r}_M \\ \boldsymbol{\vartheta}_M \end{bmatrix} \quad , \tag{11}$$

where $\mathbf{F}_{St}$ and $\mathbf{M}_{St}$ are the stiffness forces and torques acting on the j-th test-mass, while $S_{TT}, S_{RT}, S_{TR}, S_{RR} \in \mathbb{R}^{3\times3}$ are the stiffness matrices that can obtained by means of CAD-based techniques [27].

3.3.4. TM attitude dynamics

The angular velocity of the j-th TM relative to the corresponding ORF in MRF components ($\boldsymbol{\omega}_{Mj}$) is given by the addition rule of the angular velocities:

$$\boldsymbol{\omega}_{Mj} = \boldsymbol{\omega}_{MIj} - T_{Oj}^{Mj}\boldsymbol{\omega}_{\gamma j} - T_S^{Mj}\boldsymbol{\omega}_{SI}, \tag{12}$$

where both the angular motions of the spacecraft $\boldsymbol{\omega}_{SI}$ and the optical assembly $\boldsymbol{\omega}_\gamma$ are considered. To improve readability, the j subscript will be omitted. The angular acceleration is given by the time derivative of (12) and by (1):

$$\begin{aligned} \dot{\boldsymbol{\omega}}_M &= \dot{\boldsymbol{\omega}}_{MI} - \dot{T}_O^M\boldsymbol{\omega}_\gamma - T_O^M\dot{\boldsymbol{\omega}}_\gamma - \dot{T}_S^M\boldsymbol{\omega}_{SI} - T_S^M\dot{\boldsymbol{\omega}}_{SI} \\ &= \dot{\boldsymbol{\omega}}_{MI} + \boldsymbol{\omega}_M \times T_O^M\boldsymbol{\omega}_\gamma - T_O^M\dot{\boldsymbol{\omega}}_\gamma + \boldsymbol{\omega}_M \times T_S^M\boldsymbol{\omega}_{SI} - T_S^M\dot{\boldsymbol{\omega}}_{SI}. \end{aligned} \tag{13}$$

The inertial angular acceleration of the test mass $\dot{\boldsymbol{\omega}}_{MI}$ in (13) is given by the Euler's equation:

$$\dot{\boldsymbol{\omega}}_{MI} = -J_M^{-1}\boldsymbol{\omega}_{MI} \times J_M\boldsymbol{\omega}_{MI} + J_M^{-1}T_O^M\left(\mathbf{M}_E + \mathbf{D}_M + \mathbf{M}_{St}\right), \tag{14}$$

where $\mathbf{M}_E$ is the torque provided by the electrostatic suspension, $\mathbf{D}_M$ is the resultant of all the disturbance torques acting on the test-mass, while $\mathbf{M}_{St} = S_{TR}\mathbf{r}_M + S_{RR}\boldsymbol{\vartheta}_M$ is the stiffness torque from (11). $T_O^M = T(\mathfrak{q}_M^*)$ and $T_S^M = T_O^M T_S^O = T(\mathfrak{q}_M^*)Z(-\gamma)$ are time-variant matrices, since they depend on the test-mass attitude quaternion and on the OA opening angle (7).

To conclude, the attitude dynamics model of the j-th TM relative to the corresponding ORF in MRF components is given by (13) and (14):

$$\begin{aligned}
\dot{\boldsymbol{\omega}}_M &= \dot{\boldsymbol{\omega}}_{MI} + \boldsymbol{\omega}_M \times T_O^M \boldsymbol{\omega}_\gamma - T_O^M \dot{\boldsymbol{\omega}}_\gamma + \boldsymbol{\omega}_M \times T_S^M \boldsymbol{\omega}_{SI} - T_S^M \dot{\boldsymbol{\omega}}_{SI} \\
\dot{\boldsymbol{\omega}}_{MI} &= -J_M^{-1}\boldsymbol{\omega}_{MI} \times J_M \boldsymbol{\omega}_{MI} + J_M^{-1} T_O^M \left(\mathbf{M}_E + \mathbf{D}_M + \mathbf{M}_{St}\right) \\
\dot{\mathfrak{q}}_M &= \frac{1}{2}\mathfrak{q}_M \otimes \boldsymbol{\omega}_{M\mathfrak{q}} = \frac{1}{2} Q(\mathfrak{q}_M)\boldsymbol{\omega}_{M\mathfrak{q}},
\end{aligned} \tag{15}$$

The TM attitude quaternion $\dot{\mathfrak{q}}_M$ is obtained from the TM angular velocity $\boldsymbol{\omega}_{M\mathfrak{q}} = (0, \boldsymbol{\omega}_M)$ by integrating the standard quaternion kinematics equation. Moreover, the attitude angles $\boldsymbol{\theta}_M$ can be obtained from the attitude quaternion through (2).

3.3.5. TM-SC translation

The position of the j-th test-mass relative to the corresponding cage center (ORF origin) in IRF coordinates is

$$\mathbf{r}_{Mj}^I = T_{Oj}^I \mathbf{r}_{Mj}. \tag{16}$$

From now on the j-th subscript will be omitted to improve readability. By performing the first two time derivatives of (16) and by considering (1), the translational velocity and acceleration are

$$\begin{aligned}
\dot{\mathbf{r}}_M^I &= \dot{T}_O^I \mathbf{r}_M + T_O^I \dot{\mathbf{r}}_M \\
&= T_O^I \boldsymbol{\omega}_O \times \mathbf{r}_M + T_O^I \dot{\mathbf{r}}_M,
\end{aligned} \tag{17}$$

$$\begin{aligned}
\ddot{\mathbf{r}}_M^I &= \dot{T}_O^I \boldsymbol{\omega}_O \times \mathbf{r}_M + T_O^I \dot{\boldsymbol{\omega}}_O \times \mathbf{r}_M + T_O^I \boldsymbol{\omega}_O \times \dot{\mathbf{r}}_M + \dot{T}_O^I \dot{\mathbf{r}}_M + T_O^I \ddot{\mathbf{r}}_M \\
&= T_O^I \boldsymbol{\omega}_O \times \boldsymbol{\omega}_O \times \mathbf{r}_M + T_O^I \dot{\boldsymbol{\omega}}_O \times \mathbf{r}_M + T_O^I \boldsymbol{\omega}_O \times \dot{\mathbf{r}}_M + T_O^I \boldsymbol{\omega}_O \times \dot{\mathbf{r}}_M + T_O^I \ddot{\mathbf{r}}_M \\
&= T_O^I \left(\boldsymbol{\omega}_O^\times \boldsymbol{\omega}_O^\times + \dot{\boldsymbol{\omega}}_O^\times\right) \mathbf{r}_M + 2 T_O^I \boldsymbol{\omega}_O \times \dot{\mathbf{r}}_M + T_O^I \ddot{\mathbf{r}}_M \\
&= T_O^I \Omega\left(\boldsymbol{\omega}_O\right) \mathbf{r}_M + 2 T_O^I \boldsymbol{\omega}_O \times \dot{\mathbf{r}}_M + T_O^I \ddot{\mathbf{r}}_M,
\end{aligned} \tag{18}$$

where $\boldsymbol{\omega}_O$ is the angular velocity of the optical assembly with respect to the IRF and it is given by $\boldsymbol{\omega}_O = \boldsymbol{\omega}_\gamma + T_S^O \boldsymbol{\omega}_{SI}$. Equation (18) shows centrifugal and Coriolis acceleration terms since the ORF is a non-inertial frame with angular velocity $\boldsymbol{\omega}_O$. Moreover, by expliciting the acceleration of the TM CoM relative to the cage center in ORF coordinates we obtain:

$$\ddot{\mathbf{r}}_M = T_I^O \ddot{\mathbf{r}}_M^I - \Omega\left(\boldsymbol{\omega}_O\right) \mathbf{r}_M - 2\boldsymbol{\omega}_O \times \dot{\mathbf{r}}_M. \tag{19}$$

On the other side, $\boldsymbol{r}_M^I$ is also given by the following sum of position vectors:

$$\mathbf{r}_M^I = \mathbf{r}_{MI} - \mathbf{r}_I - T_S^I \mathbf{b}_S - T_O^I \mathbf{b}_M, \tag{20}$$

where $\mathbf{r}_{MI}$ is the distance between the test mass and the IRF origin, $\mathbf{r}_I$ is the distance between the SRF and the IRF origin, $\mathbf{b}_S$ is the distance between the SRF and the pivot of the optical assembly, $\mathbf{b}_M$ is the distance between the pivot and the cage center. By performing the second time derivative of (20) and by considering (1), the velocity and the acceleration of the test-mass relative to the cage center in IRF coordinates can be also written as:

$$\begin{aligned} \dot{\mathbf{r}}_M^I &= \dot{\mathbf{r}}_{MI} - \dot{\mathbf{r}}_I - \dot{T}_S^I \mathbf{b}_S - \dot{T}_O^I \mathbf{b}_M \\ &= \dot{\mathbf{r}}_{MI} - \dot{\mathbf{r}}_I - T_S^I \boldsymbol{\omega}_{SI} \times \mathbf{b}_S - T_O^I \boldsymbol{\omega}_O \times \mathbf{b}_M, \end{aligned} \tag{21}$$

$$\begin{aligned} \ddot{\mathbf{r}}_M^I &= \ddot{\mathbf{r}}_{MI} - \ddot{\mathbf{r}}_I - \dot{T}_S^I \boldsymbol{\omega}_{SI} \times \mathbf{b}_S - T_S^I \dot{\boldsymbol{\omega}}_{SI} \times \mathbf{b}_S - \dot{T}_O^I \boldsymbol{\omega}_O \times \mathbf{b}_M - T_O^I \dot{\boldsymbol{\omega}}_O \times \mathbf{b}_M \\ &= \ddot{\mathbf{r}}_{MI} - \ddot{\mathbf{r}}_I - T_S^I \boldsymbol{\omega}_{SI} \times \boldsymbol{\omega}_{SI} \times \mathbf{b}_S - T_S^I \dot{\boldsymbol{\omega}}_{SI} \times \mathbf{b}_S - T_O^I \boldsymbol{\omega}_O \times \boldsymbol{\omega}_O \times \mathbf{b}_M - T_O^I \dot{\boldsymbol{\omega}}_O \times \mathbf{b}_M \\ &= \ddot{\mathbf{r}}_{MI} - \ddot{\mathbf{r}}_I - T_S^I \left(\boldsymbol{\omega}_{SI}^{\times} \boldsymbol{\omega}_{SI}^{\times} + \dot{\boldsymbol{\omega}}_{SI}^{\times} \right) \mathbf{b}_S - T_O^I \left(\boldsymbol{\omega}_O^{\times} \boldsymbol{\omega}_O^{\times} + \dot{\boldsymbol{\omega}}_O^{\times} \right) \mathbf{b}_M \\ &= \ddot{\mathbf{r}}_{MI} - \ddot{\mathbf{r}}_I - T_S^I \Omega \left(\boldsymbol{\omega}_{SI} \right) \mathbf{b}_S - T_O^I \Omega \left(\boldsymbol{\omega}_O \right) \boldsymbol{b}_M, \end{aligned} \tag{22}$$

where $\dot{\mathbf{b}}_S = \dot{\mathbf{b}}_M = \mathbf{0}$ since $\mathbf{b}_S$ and $\mathbf{b}_M$ are constant distances. The inertial acceleration of the j-th test-mass $\ddot{\mathbf{r}}_{MI}$ and the inertial acceleration of the spacecraft $\ddot{\mathbf{r}}_I$ can be obtained by means of the Newton's Law:

$$\begin{aligned} \ddot{\mathbf{r}}_{MI} &= -\mu_{\odot} \frac{\mathbf{r}_{MI}}{|\mathbf{r}_{MI}|^3} + m_M^{-1} T_O^I (\mathbf{F}_E + \mathbf{d}_M + \mathbf{F}_{St}) \\ \ddot{\mathbf{r}}_I &= -\mu_{\odot} \frac{\mathbf{r}_I}{|\mathbf{r}_I|^3} + m_S^{-1} T_S^I (\mathbf{F}_T + \mathbf{d}_S) - m_S^{-1} \sum_{j=1,2} T_{Oj}^I \left(\mathbf{F}_{Ej} \right), \end{aligned} \tag{23}$$

where $\mathbf{F}_T + \mathbf{d}_S$ are the resultant force of the thrusters and of the external disturbances acting on the spacecraft body. The term $-m_S^{-1} \sum_{j=1,2} T_{Oj}^I \left(\mathbf{F}_{Ej} \right)$ are the reaction forces of the two electrostatic suspensions on the spacecraft, when $j = 1$ the subscript can be omitted. $\mathbf{d}_M$ is the resultant of the disturbance forces acting on the test-mass, while $\mathbf{F}_{St} = S_{TT} \mathbf{r}_M + S_{RT} \boldsymbol{\vartheta}_M$ are the stiffness forces from (11).

By replacing (23) into (22), we have the complete expression of the test mass acceleration relative to the cage center in IRF coordinates:

$$\begin{aligned} \ddot{\mathbf{r}}_M^I &= K_{\Delta} \Delta \mathbf{r}_I + m_M^{-1} T_O^I (\mathbf{F}_E + \mathbf{d}_M + \mathbf{F}_{St}) - m_S^{-1} T_S^I (\mathbf{F}_T + \mathbf{d}_S) \\ &\quad + m_S^{-1} \sum_{j=1,2} T_{Oj}^I \mathbf{F}_{Ej} - T_S^I \Omega \left(\boldsymbol{\omega}_{SI} \right) \mathbf{b}_S - T_O^I \Omega \left(\boldsymbol{\omega}_O \right) \boldsymbol{b}_M, \end{aligned} \tag{24}$$

where:

$$K_{\Delta} \Delta \mathbf{r}_I \cong -\mu_{\odot} \left(\frac{\mathbf{r}_{MI}}{|\mathbf{r}_{MI}|^3} - \frac{\mathbf{r}_I}{|\mathbf{r}_I|^3} \right),$$

is the spacecraft/test-mass gravity gradient.

By replacing (24) into (19), we obtain the complete expression of the test mass acceleration relative to the cage center in ORF coordinates:

$$\ddot{\mathbf{r}}_M = T_I^O \left(K_\Delta \Delta \mathbf{r}_I + m_M^{-1} T_O^I (\mathbf{F}_E + \mathbf{d}_M + \mathbf{F}_{St}) - m_S^{-1} T_S^I (\mathbf{F}_T + \mathbf{d}_S) \right.$$
$$\left. + m_S^{-1} \sum_{j=1,2} T_{Oj}^I \mathbf{F}_{Ej} - T_S^I \Omega(\boldsymbol{\omega}_{SI}) \mathbf{b}_S - T_O^I \Omega(\boldsymbol{\omega}_O) \mathbf{b}_M \right) - \Omega(\boldsymbol{\omega}_O) \mathbf{r}_M - 2\boldsymbol{\omega}_O \times \dot{\mathbf{r}}_M. \tag{25}$$

To sum up, the TM translation model can be expressed as follows:

$$\begin{aligned}
\ddot{\mathbf{r}}_M &= \mathbf{a}_N - T_S^O \Omega(\boldsymbol{\omega}_{SI}) \mathbf{b}_S - \Omega(\boldsymbol{\omega}_O) \mathbf{b}_M - \Omega(\boldsymbol{\omega}_O) \mathbf{r}_M - 2\boldsymbol{\omega}_O \times \dot{\mathbf{r}}_M \\
\mathbf{a}_N &= T_I^O K_\Delta \Delta \mathbf{r}_I + m_M^{-1} (\mathbf{F}_E + \mathbf{d}_M + \mathbf{F}_{St}) - m_S^{-1} T_S^O (\mathbf{F}_T + \mathbf{d}_S) + m_S^{-1} \sum_{j=1,2} T_{Oj}^O \mathbf{F}_{Ej} \\
\Omega(\boldsymbol{\omega}_O) &= \boldsymbol{\omega}_O^\times \boldsymbol{\omega}_O^\times + \dot{\boldsymbol{\omega}}_O^\times \\
\boldsymbol{\omega}_O &= T_S^O \boldsymbol{\omega}_{SI} + \boldsymbol{\omega}_\gamma \\
\dot{\boldsymbol{\omega}}_O &= \dot{T}_S^O \boldsymbol{\omega}_{SI} + T_S^O \dot{\boldsymbol{\omega}}_{SI} + \dot{\boldsymbol{\omega}}_\gamma = -\boldsymbol{\omega}_\gamma \times T_S^O \boldsymbol{\omega}_{SI} + T_S^O \dot{\boldsymbol{\omega}}_{SI} + \dot{\boldsymbol{\omega}}_\gamma,
\end{aligned} \tag{26}$$

where $\ddot{\mathbf{r}}_M$ is TM acceleration relative to the cage center in ORF coordinates, $\mathbf{a}_N$ collects all the terms related to the forces, $\boldsymbol{\omega}_O$ is the ORF angular velocity. When $j = 1$, the subscript can be omitted and consequently the rotation matrix T_O^O is the identity matrix, while T_{O2}^O is rotation matrix from ORF2 to ORF1. The rotation matrices T_S^O, T_{O2}^O are time-variant being a function of the angle $\gamma(t)$.

To conclude this section, it is worth noticing that (8) (10) (15) (26) are all coupled together.

4. Validation

4.1. Linear Analysis

The most important activity when validating models for complex systems is to check that the main dynamics are accurately represented. In this case, real data were not available and a Matlab Simscape multibody model was used as a benchmark. SimScape is a CAD-like software based on Matlab/Simulink, allowing to build models of complex physical systems using a set of elementary blocks, thus avoiding the use of mathematical equations. Although the SimScape model is accurate in simulating the spacecraft dynamics, it does not provide a mathematical description of the system that is being modeled. As already mentioned in Section 3.1, LISA is a 20x17 MIMO system, where the input and output vectors are

$$\boldsymbol{u} = \begin{pmatrix} \mathbf{F}_T & \mathbf{M}_T & \mathrm{M}_{OA1} & \mathrm{M}_{OA2} & \mathbf{F}_{E1} & \mathbf{M}_{E1} & \mathbf{F}_{E2} & \mathbf{M}_{E2} \end{pmatrix} \in \mathbb{R}^{20}$$

$$\boldsymbol{y} = \begin{pmatrix} \boldsymbol{\theta}_{SI} & \mathbf{r}_{M1} & \boldsymbol{\theta}_{M1} & \mathbf{r}_{M2} & \boldsymbol{\theta}_{M2} & \zeta_1 & \zeta_2 \end{pmatrix} \in \mathbb{R}^{17},$$

$$\boldsymbol{x} = \begin{pmatrix} \boldsymbol{\theta}_{SI} & \mathbf{r}_{M1} & \boldsymbol{\theta}_{M1} & \mathbf{r}_{M2} & \boldsymbol{\theta}_{M2} & \zeta_1 & \zeta_2 & \dot{\boldsymbol{\theta}}_{SI} & \dot{\mathbf{r}}_{M1} & \dot{\boldsymbol{\theta}}_{M1} & \dot{\mathbf{r}}_{M2} & \dot{\boldsymbol{\theta}}_{M2} & \dot{\zeta}_1 & \dot{\zeta}_2 \end{pmatrix} \in \mathbb{R}^{34},$$

where $\boldsymbol{\theta}_{SI}$, $\boldsymbol{\theta}_{M1}$, $\boldsymbol{\theta}_{M2}$ are the Euler 123 angles. A first comparison between the benchmark and the analytical model could be carried out in the frequency domain. The first step consists in linearizing both models around the same working point, given by

$$\overline{\boldsymbol{x}} = \mathbf{0},$$

obtaining 340 unstable transfer functions G for each model, which are unstable and consequently have an infinite DC-gain:

$$\boldsymbol{y} = G\boldsymbol{u}, \qquad G \in \mathbb{R}^{17\times 20}.$$

It is worth noticing that the comparison in the frequency domain is difficult, since the standard system norms (e.g., the H-infinity and H-2 norms) cannot be used due to system instability. To overcome this issue, we propose the following approach. Given $G_0 \in \mathbb{R}^{17\times 20}$ the set of transfer functions of the Simscape model, a way to identify the most relevant contributions acting on the j-th output is:

$$\begin{aligned}
\widehat{G}_0 &= \max\left(G_0(j\omega)\right), \text{ where } \quad 2\pi\cdot 10^{-5} \leq \omega \leq 2\pi \cdot 10^{0} \quad \text{(LISA bandwidth)} \\
\overline{u} &= \begin{pmatrix} \overline{\mathbf{F}}_T & \overline{\mathbf{M}}_T & \overline{\mathrm{M}}_{OA1} & \overline{\mathrm{M}}_{OA2} & \overline{\mathbf{F}}_{E1} & \overline{\mathbf{M}}_{E1} & \overline{\mathbf{F}}_{E2} & \overline{\mathbf{M}}_{E2} \end{pmatrix} \\
M_0 &= \widehat{G}_0 \overline{u},
\end{aligned}$$

where $\widehat{G}_0 \in \mathbb{R}^{17\times 20}$ are the peak magnitudes of all the transfer functions on the LISA frequency range, $\overline{u}$ are the input amplitudes of the LISA actuators $\overline{\mathrm{F}}_T = 1\cdot 10^{-5}$ N, $\overline{\mathrm{M}}_T = 2\cdot 10^{-5}$ Nm, $\overline{\mathrm{M}}_{OA} = 1\cdot 10^{-2}$ Nm, $\overline{\mathrm{F}}_{E1} = \overline{\mathrm{F}}_{E2} = 5.7\cdot 10^{-9}$ N, $\overline{\mathrm{M}}_{E1} = \overline{\mathrm{M}}_{E2} = 3\cdot 10^{-11}$ Nm. The product between $\widehat{G}_0$ and $\overline{u}$ provides map M_0 that can be normalized column-wise:

$$\mathrm{M}_0\left(i\,,j\right) = \frac{\mathrm{M}_0\left(i\,,j\right)}{\max_{k=1:20}\left(\mathrm{M}_0\left(k\,,j\right)\right)} \quad \forall i = 1:20,\ j = 1:17.$$

M_0 identifies the relevant transfer functions of the Simscape model. In turn, this implies a unitary value for the most important dynamic acting on the j-th output. The obtained results are shown in Figure 6. It is interesting to notice how the first three inputs (related to the thruster force $\overline{\mathbf{F}}_T$), mainly act on outputs 4,5,6 and 10,11,12 (TM1 and TM2 translations with respect to their cage centers). Inputs 4-5-6 (thruster torques $\overline{\mathbf{M}}_T$) mainly act on output 1, 2, 3 (spacecraft attitude). Input 7 and 8 (optical assembly torques $\overline{\mathrm{M}}_{OA1}, \overline{\mathrm{M}}_{OA2}$), mainly act on output 16-17 (OA zeta angles). Or again, inputs 9-10-11 and 15-16-17 (electrostatic suspension forces) are not unitary values since the main dynamics acting on the test mass translation is given by the thrusters.

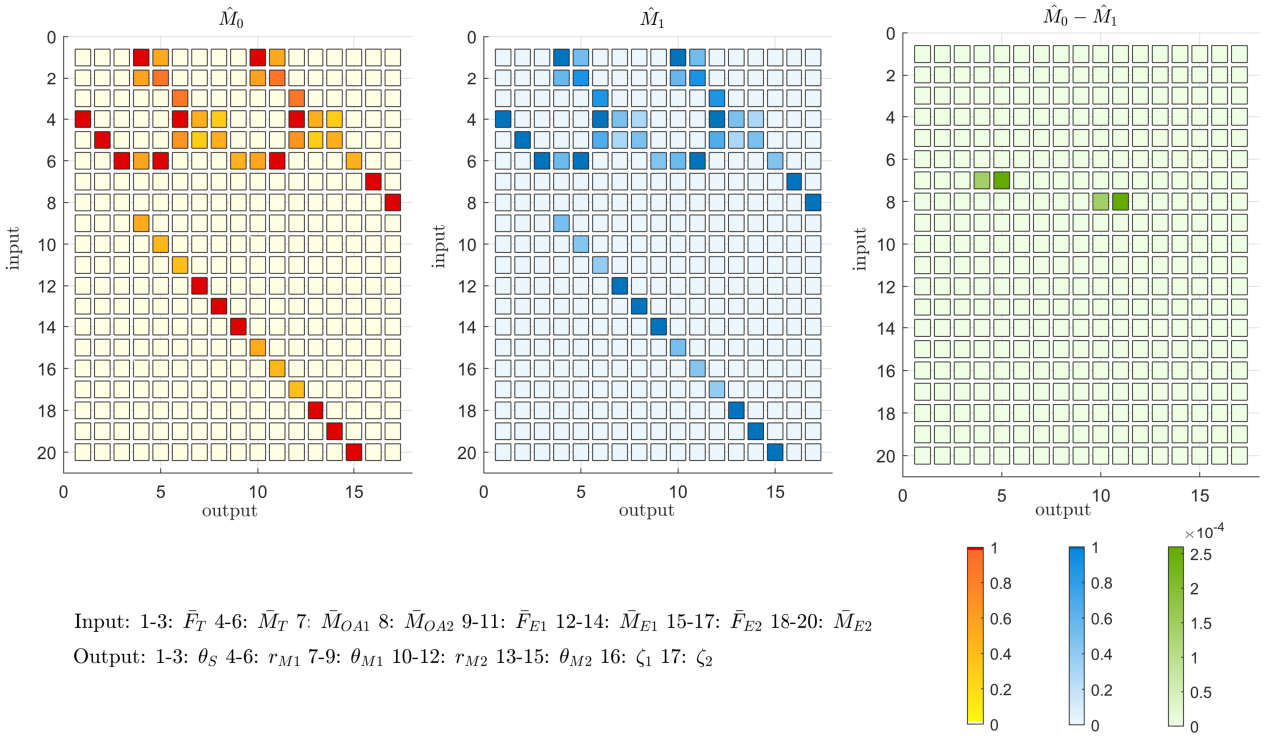

Figure 6: Most important transfer functions of the LISA system (Left: SimScape $\hat{\mathrm{M}}_0$, Center: Analytical $\hat{\mathrm{M}}_1$, Right: $\hat{\mathrm{M}}_0 - \hat{\mathrm{M}}_1$.

The same procedure was repeated for the analytical model, but in this case the column normalization of map $\mathrm{M}_1 = \widehat{\mathrm{G}}_1 \bar{\mathrm{u}}$ is performed with respect to the maxima of map M_0, in order to have a common scaling reference necessary to evaluate the modelling errors:

$$\hat{\mathrm{M}}_1(i,j) = \frac{\mathrm{M}_1(i,j)}{\max_{k=1:20}(\mathrm{M}_0(k,j))} \quad \forall i = 1:20,\ j = 1:17,$$

Finally, the modelling error on the main dynamics in the frequency range of interest is evaluated as the difference between the two maps: $e = \hat{\mathrm{M}}_0 - \hat{\mathrm{M}}_1$. The obtained results are reported in Figure 6 and in Table 3. The highest modelling error is lower than $3 \cdot 10^{-4}$ and it occurs on the transfer functions that relate the OA command torques to the test-mass x-y positions. These results are acceptable being small values. Thus, we can conclude that the relevant transfer functions are correctly modelled. The zero values are those related to the transfer functions that are null both on the Simscape and the analytical model.

4.2. Simulations

The drawback of the linear analysis is that the linearization process neglects the plant nonlinearities, which are an important element of the spacecraft dynamics and of our model. Hence, a second validation was carried out in order to compare the two models in conditions where the contribution of the nonlinearities is not negligible. It must be remarked that small initial errors (even numerical) between the two models could diverge to infinite for long simulation horizons, since all the transfer functions are unstable. Many of them are double integrators and thus have a slope of -40 db/dec and an infinite DC gain. Figure 7 shows an example of open loop simulation. Plots on the left column show the system output of both the Simscape and the analytical model. Continuous

and dashed lines are overlapped, meaning that the output errors are very small as shown in the plots of the right column. It should be noted that the error evolution follows a quadratic law, since the system is unstable.

As a further evaluation, Table 4 summarizes the arithmetic mean and the root mean square output errors of a Monte-Carlo campaign made of 1000 open loop runs. Constant inputs were randomly chosen between the saturations of the actuators. The simulation horizon was set to 100 s, which can be considered enough since the models will be used for the design of closed loop controls. Despite system instability, the obtained RMSE are generally small between 10^{-19} and 10^{-9} orders of magnitude depending on the degree of freedom, demonstrating a satisfactory modelling accuracy.

5. Conclusions

The LISA mission will be of primary importance for the detection of gravitational waves in the $\left[1 \cdot 10^{-5}, 1\right]$ Hz bandwidth. The current spacecraft concept consists of a main body carrying two moving optical assemblies and two suspended test-masses, resulting in a MIMO system with 20 inputs and 17 outputs. From the control design point of view, it is important to obtain an analytical model which is a good trade-off between accuracy and complexity. In the present paper, a set of reference systems was defined and then a nonlinear model based on the Newton-Euler approach was derived. To validate the model, frequency and time domain comparisons with a Matlab-Simscape multibody model were carried out. At first, both models were linearized around the same working point. Then, the main system dynamics were identified by searching for the peak magnitudes of every transfer function in the LISA frequency range and by multiplying them for the command amplitude. The same procedure was repeated for the analytical model and finally the two maps were compared to identify modeling errors. The findings showed very small errors between the two maps, with a maximum value lower than $3 \cdot 10^{-4}$ on the dynamics relating the optical assembly torques with the x-y positions of the test-masses. Finally, the two models were compared also in the time domain, by evaluating the open loop output error given the same input. To this aim, a Monte-Carlo test campaign based on 1000 simulations was carried out and the mean output error was evaluated for each output variable. The obtained output errors were generally small between 10^{-19} and 10^{-9} orders of magnitude depending on the degree of freedom, despite the system instability and a relatively long simulation horizon of 100s. To conclude, the model here presented proved to be accurate and suitable for future works such the analytical linearization and decoupling as well as the analysis and control design of the LISA mission.

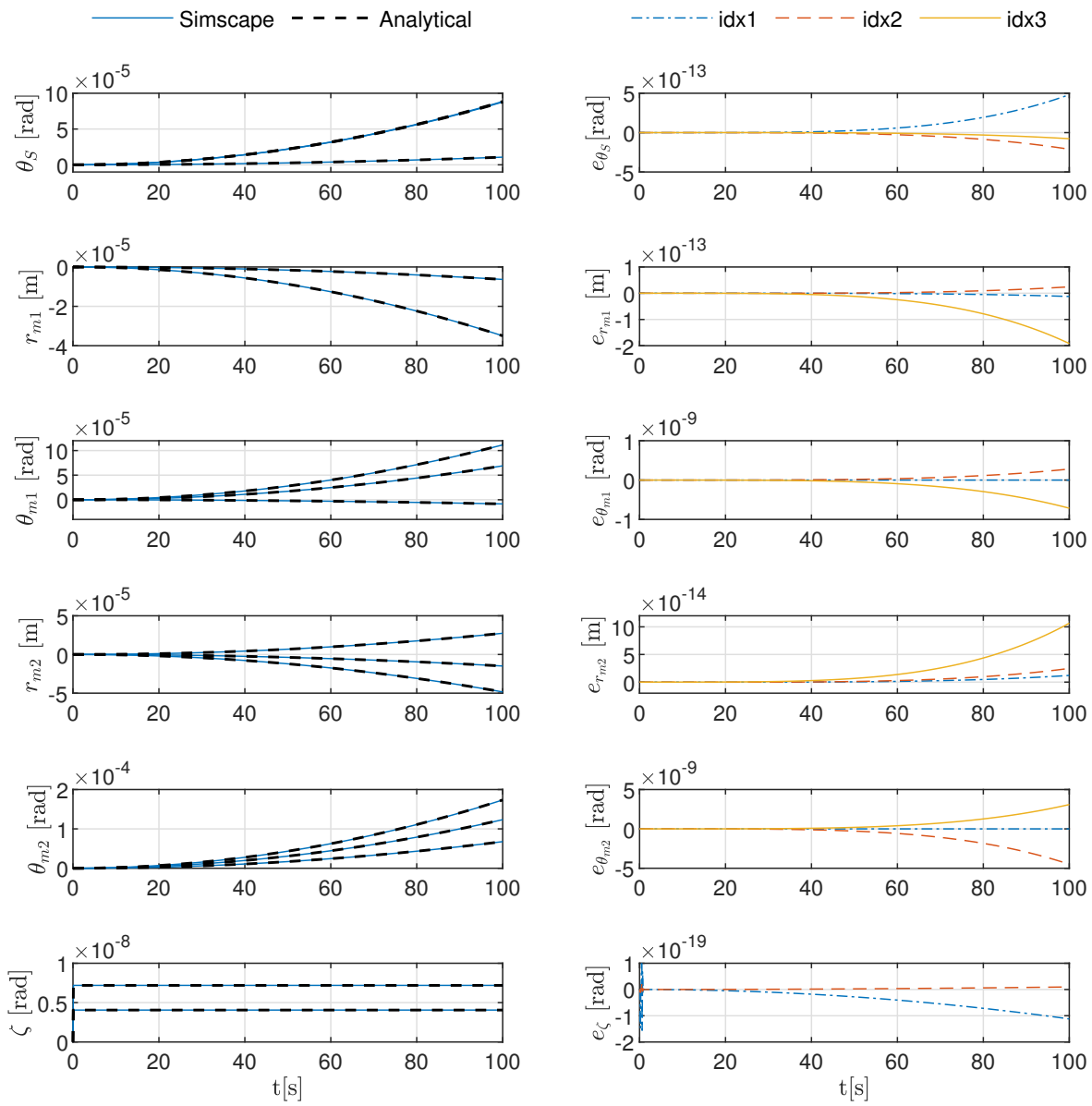

Figure 7: Example of open loop comparison. In the plots on the left, the Simscape outputs are almost overlapped by the analytical model. Indeed, the plots on the right show very small errors between the two models. The error evolution follows a quadratic law, since the systems are unstable. Therefore, initial errors (even numerical) increase quadratically over time in open loop. Idx1-2-3 stands for the first, second and third component of the considered vector.

	$\boldsymbol{\theta}_{SI}$			$\mathbf{r}_{M1}$			$\boldsymbol{\theta}_{M1}$			$\mathbf{r}_{M2}$			$\boldsymbol{\theta}_{M2}$			ζ_1	ζ_2
$\mathbf{F}_T$	0	0	0	1.1e-15	0	0	0	0	0	7.8e-16	2.2e-16	0	0	0	0	0	0
	3.0e-52	5.1e-36	2.4e-18	0	7.8e-16	3.3e-36	1.7e-34	2.1e-36	1.1e-18	0	6.7e-16	7.1e-17	1.7e-34	1.9e-36	1.1e-18	8.1e-23	8.1e-23
	0	0	0	0	0	5.6e-16	0	0	0	0	0	5.6e-16	0	0	0	0	0
$\mathbf{M}_T$	8.3e-11	0	0	0	0	4.4e-16	4.2e-11	2.4e-11	0	0	0	4.4e-16	4.2e-11	2.4e-11	0	0	0
	3.5e-50	8.3e-11	7.2e-18	4.0e-18	7.2e-18	2.2e-16	2.4e-11	4.2e-11	9.4e-17	4.0e-18	7.2e-18	2.2e-16	2.4e-11	4.2e-11	9.4e-17	7.0e-21	7.0e-21
	1.7e-34	2.1e-18	1.5e-09	6.9e-09	3.8e-09	7.2e-17	1.3e-18	2.3e-17	3.8e-11	1.1e-08	4.0e-09	1.8e-34	4.2e-19	2.5e-17	3.8e-11	1.1e-19	1.1e-19
M_{OA1}	1.6e-14	3.2e-14	3.6e-14	**1.4e-04**	**2.6e-04**	5.6e-14	3.1e-15	8.6e-32	3.0e-12	9.5e-14	1.7e-13	2.1e-14	1.4e-14	3.6e-14	8.9e-14	1.4e-15	3.9e-18
M_{OA2}	1.6e-14	3.2e-14	3.5e-14	3.9e-14	1.7e-13	5.6e-14	2.8e-14	1.4e-14	1.3e-21	**1.4e-04**	**2.6e-04**	2.1e-14	1.0e-14	1.2e-31	1.1e-12	5.6e-18	3.2e-15
$\mathbf{F}_{E1}$	1.4e-39	9.8e-23	1.3e-12	2.3e-13	2.1e-13	6.4e-23	5.8e-23	4.1e-23	1.7e-15	2.2e-13	4.0e-13	5.9e-39	1.9e-23	3.6e-23	1.7e-15	4.3e-24	4.1e-24
	6.8e-39	2.0e-22	6.3e-13	9.7e-13	8.0e-13	8.0e-20	1.2e-22	8.3e-23	3.5e-15	4.5e-13	8.1e-13	8.0e-20	3.8e-23	7.3e-23	3.5e-15	6.6e-24	8.7e-24
	7.1e-15	4.8e-15	2.6e-22	1.4e-22	2.6e-22	1.1e-16	2.2e-15	4.4e-15	3.6e-21	1.4e-22	2.6e-22	4.9e-19	4.9e-15	3.2e-16	6.8e-21	8.7e-27	5.0e-25
$\mathbf{M}_{E1}$	1.1e-16	6.2e-17	0	1.4e-22	1.2e-22	6.4e-22	8.3e-11	1.0e-22	0	2.8e-22	2.5e-22	6.4e-22	3.6e-17	6.2e-17	0	0	0
	6.2e-17	1.1e-16	1.4e-39	1.5e-30	2.5e-22	4.2e-22	4.4e-23	8.3e-11	1.5e-22	2.6e-23	1.5e-23	2.9e-22	6.2e-17	3.6e-17	1.5e-22	1.1e-26	1.1e-26
	4.7e-23	9.2e-23	1.2e-16	4.2e-13	7.5e-13	6.0e-23	2.5e-23	1.3e-24	8.3e-11	2.9e-18	1.7e-17	6.2e-23	4.2e-23	6.9e-23	5.8e-17	1.2e-24	5.2e-26
$\mathbf{F}_{E2}$	1.4e-39	9.8e-23	1.3e-12	2.2e-13	4.0e-13	6.4e-23	5.8e-23	4.1e-23	1.7e-15	2.2e-13	4.0e-13	5.9e-39	1.9e-23	3.6e-23	1.7e-15	4.3e-24	4.1e-24
	6.8e-39	2.0e-22	6.3e-13	4.5e-13	8.1e-13	8.0e-20	1.2e-22	8.3e-23	3.5e-15	5.0e-13	8.2e-13	4.0e-20	3.8e-23	7.3e-23	3.5e-15	6.6e-24	8.7e-24
	7.1e-15	4.8e-15	0	0	0	4.9e-19	4.9e-15	3.2e-16	7.0e-21	0	0	1.1e-16	2.2e-15	4.4e-15	0	0	0
$\mathbf{M}_{E2}$	1.1e-16	6.2e-17	2.7e-24	2.7e-22	2.7e-24	6.4e-22	3.6e-17	6.2e-17	1.2e-24	1.4e-22	1.3e-22	6.4e-22	8.3e-11	1.0e-22	1.2e-24	5.3e-27	9.2e-29
	6.2e-17	1.1e-16	5.4e-24	5.6e-24	2.1e-23	2.9e-22	6.2e-17	3.6e-17	2.5e-24	3.0e-24	2.4e-22	4.2e-22	4.4e-23	8.3e-11	7.1e-23	1.8e-28	1.1e-26
	4.7e-23	9.2e-23	1.2e-16	6.8e-18	1.4e-17	6.0e-23	8.3e-23	7.8e-23	5.8e-17	4.2e-13	7.5e-13	6.2e-23	6.6e-24	1.2e-24	8.3e-11	1.2e-25	6.6e-24

Table 3: Errors between the analytical and the Simscape model obtained by subtracting map $\hat{\mathrm{M}}_0$ with map $\hat{\mathrm{M}}_1$.

Output	$\boldsymbol{\theta}_{SI}$ [rad]			$\mathbf{r}_{M1}$ [m]			$\boldsymbol{\theta}_{M1}$ [rad]			$\mathbf{r}_{M2}$ [m]			$\boldsymbol{\theta}_{M2}$ [rad]			ζ_1 [rad]	ζ_2 [rad]
AME	8.6e-14	-1.3e-13	-8.3e-14	-1.2e-14	2.4e-14	-5.5e-14	1.2e-13	-4.7e-10	-1.2e-9	1.2e-14	2.4e-14	1.1e-16	-1.5e-13	-1.5e-9	1.2e-9	-2.2e-20	-7.3e-20
RMSE	1.6e-13	1.8e-13	1.3e-13	2.0e-14	4.1e-14	7.8e-14	2.5e-13	1.5e-9	1.9e-9	2.0e-14	4.1e-14	3.9e-14	2.4e-13	2.3e-9	1.8e-9	8.8e-20	1.1e-19

Table 4: Mean output errors.

Funding source

This work was funded by the European Space Agency. The Authors ensure complete objectivity in the data interpretation and writing of the paper. The view expressed in this work cannot be taken as the official position of the European Space Agency.

References

[1] J. Aasi *et al.*, "Advanced LIGO," *Classical and Quantum Gravity*, vol. 32, p. 074001, Mar 2015.

[2] B. P. Abbott *et al.*, "Observation of gravitational waves from a binary black hole merger," *Phys. Rev. Lett.*, vol. 116, p. 061102, Feb 2016.

[3] P. Amaro-Seoane *et al.*, "Laser Interferometer Space Antenna," *arXiv e-prints*, p. arXiv:1702.00786, Feb 2017.

[4] K. Danzmann *et al.*, "LISA (Laser Interferometer Space Antenna) Proposal for a Laser-Interferometric Gravitational Wave Detector in Space," *MPQ-Reports*, vol. 177, 1993.

[5] F. Antonucci *et al.*, "The LISA Pathfinder mission," *Classical and Quantum Gravity*, vol. 29, p. 124014, Jun 2012.

[6] L. Giulicchi *et al.*, "Attitude and orbit control systems for the LISA Pathfinder mission," *Aerospace Science and Technology*, vol. 24, no. 1, pp. 283 – 294, 2013.

[7] M. Diaz-Aguilo' *et al.*, "Design of the magnetic diagnostics unit onboard LISA Pathfinder," *Aerospace Science and Technology*, vol. 26, no. 1, pp. 53 – 59, 2013.

[8] M. Armano *et al.*, "Beyond the required LISA free-fall performance: New LISA pathfinder results down to 20 uhz," *Phys. Rev. Lett.*, vol. 120, p. 061101, Feb 2018.

[9] J. Zhang, J. D. Biggs, D. Ye, and Z. Sun, "Finite-time attitude set-point tracking for thrust-vectoring spacecraft rendezvous," *Aerospace Science and Technology*, vol. 96, p. 105588, 2020.

[10] Y. Wang and H. Ji, "Integrated relative position and attitude control for spacecraft rendezvous with iss and finite-time convergence," *Aerospace Science and Technology*, vol. 85, pp. 234 – 245, 2019.

[11] X. Liu, Z. Meng, and Z. You, "Adaptive collision-free formation control for under-actuated spacecraft," *Aerospace Science and Technology*, vol. 79, pp. 223 – 232, 2018.

[12] D. Lee, "Nonlinear disturbance observer-based robust control for spacecraft formation flying," *Aerospace Science and Technology*, vol. 76, pp. 82 – 90, 2018.

[13] M. Azimi and G. Sharifi, "A hybrid control scheme for attitude and vibration suppression of a flexible spacecraft using energy-based actuators switching mechanism," *Aerospace Science and Technology*, vol. 82-83, pp. 140 – 148, 2018.

[14] Y. Zhang and X. Guan, "Active damping control of flexible appendages for spacecraft," *Aerospace Science and Technology*, vol. 75, pp. 237 – 244, 2018.

[15] A. Allasio *et al.*, "Goce mission: Design phases and in-flight experiences," vol. 137, 02 2010.

[16] B. Tapley *et al.*, "The gravity recovery and climate experiment: Mission overview and early results," *Geophysical Research Letters*, vol. 31, p. 4 PP., 05 2004.

[17] H. Klotz *et al.*, "Drag-free, attitude and orbit control for LISA," in *Spacecraft Guidance, Navigation and Control Systems*, vol. 381 of *ESA Special Publication*, p. 695, Feb 1997.

[18] P. Gath *et al.*, "Drag free and attitude control system design for the LISA science mode," *AIAA Guidance, Navigation and Control Conference and Exhibits*, 2007.

[19] P. Gath *et al.*, "Drag free and attitude control system design for the LISA pathfinder mission," in *AIAA Guidance, Navigation and Control Conference and Exhibits*, vol. 5, 08 2004.

[20] P. Gath *et al.*, "Feedback controller design for the basic science mode of the LISA Pathfinder mission," *IFAC Proceedings Volumes*, vol. 37, no. 6, pp. 839 – 844, 2004. 16th IFAC Symposium on Automatic Control in Aerospace 2004, Saint-Petersburg, Russia, 14-18 June 2004.

[21] M. Nofrarias *et al.*, "State space modelling and data analysis exercises in LISA pathfinder," 06 2013.

[22] L. Colangelo *et al.*, "LISA L3 gravity wave observatory: non-linear modelling and possible DFAC methods," in *69th International Aerospace Conference*, no. IAC-18,C1,6,4,x47173, Oct. 2018.

[23] M. Armano *et al.*, "The LISA Pathfinder mission," *Journal of Physics: Conference Series*, vol. 610, p. 012005, may 2015.

[24] A. Schleicher *et al.*, "In-orbit performance of the LISA Pathfinder drag-free and attitude control system," *CEAS Space Journal*, vol. 10, Apr. 2018.

[25] ESA, "LISA yellow book, assessment study report," tech. rep., ESA, 2011.

[26] T. Ziegler and W. Fichter, "Test mass stiffness estimation for the LISA Pathfinder drag-free system," in *AIAA Guidance, Navigation and Control Conference and Exhibit*, 2007.

[27] S. M. Merkowitz *et al.*, "Current LISA spacecraft design," *Journal of Physics: Conference Series*, vol. 154, p. 012021, mar 2009.

[28] D. Gerardi *et al.*, "Invited article: Advanced drag-free concepts for future space-based interferometers: acceleration noise performance," *Review of Scientific Instruments*, vol. 85, no. 1, p. 011301, 2014.

[29] R. Featherstone, *Rigid Body Dynamics Algorithms*. Springer-Verlag GmbH, 2008.

[30] L. Markley and J. Crassidis, *Fundamentals of Spacecraft Attitude Determination and Control*. 01 2014.